

¹ Center for Analysis and Prediction of Storms, University of Oklahoma, Norman OK 73019

² School of Meteorology University of Oklahoma, Norman OK 73019

The Advanced Regional Prediction System (ARPS) – A multi-scale nonhydrostatic atmospheric simulation and prediction tool. Part II: Model physics and applications

M. Xue^{1,2}, K. K. Droegemeier^{1,2}, V. Wong¹, A. Shapiro^{1,2}, K. Brewster¹, F. Carr^{1,2}, D. Weber¹, Y. Liu¹, and D. Wang¹

With 13 Figures

Received April 14, 2000

Revised July 17, 2000

Summary

In Part I of this paper series, the dynamic equations, numerical solution procedures and the parameterizations of subgrid-scale and PBL turbulence of the Advanced Regional Prediction System (ARPS) were described. The dynamic and numerical framework of the model was verified using idealized and real mountain flow cases and an idealized density current. In this Part II, we present the treatment of other physics processes and the related verifications.

The PBL and surface layer parameterization, the soil model and the atmospheric radiation packages are tested in a fully coupled mode to simulate the development and evolution of the PBL over a 48-hour period, using the Wangara day-33 data. A good agreement is found between the simulated and observed PBL evolution, at both day and night times.

The model is used to simulate a 3-D supercell storm that is well documented in previous literature. The results show that considerable errors can result from the use of conventional non-conservative advection schemes; the ice microphysics option coupled with a monotonic advection scheme yields the most realistic simulation with better prediction of precipitation.

The ARPS is also applied to the 48-hour prediction of a January 1999 case that involves an outbreak of a historical number of tornadoes for the month within the state of Arkansas, the United States. A long-lasting intense squall line developed following the tornado outbreak. Simulation on 32-km and 6-km resolution grids successfully reproduced the observed development and evolution, including the timing and location, of these systems. Preliminary analyses show that large-scale forcing provided the primary focusing

mechanism in triggering the initial convection in Arkansas before the outbreak of tornadic thunderstorms. It is also found that the mesoscale circulation induced by the intense long-lived squall line at the later time contributed significantly, through vertical momentum transport and geostrophic adjustment processes, to the intensification and northward propagation of upper-level jet core, which in turn influenced the evolution of surface cyclone and associated precipitation. This last set of experiments serves to demonstrate the capabilities of the ARPS as a complete system in an NWP setting. The result of these experiments and those presented in Part I establishes the credibility of the model for a wide range of applications.

1. Introduction

A completely new nonhydrostatic model system known as the Advanced Regional Prediction System (ARPS) has been developed in recent years at the Center for Analysis and Prediction of Storms (CAPS) at the University of Oklahoma. The ARPS is to serve as an effective tool for research and a system suitable for explicit prediction of convective storms and weather systems at other scales. The ARPS includes its own data ingest, quality control and objective analysis packages, a data assimilation system which includes single-Doppler velocity and thermodynamic retrieval algorithms, the forward prediction

component, and a self-contained post-processing, diagnostic and verification package.

In Part I of this paper series (Xue et al., 2000, referred to as Part I hereafter), the dynamic and numerical framework of the ARPS and the subgrid-scale and the PBL turbulence parameterizations are described. The model is then verified using idealized and real mountain flow cases as well as an idealized density current. In this second part, the treatment of the land surface processes, the coupling of PBL with the land surface model and the treatment of explicit and parameterized precipitation processes are presented, followed by verifications against observed data. Applications of the model to the simulation of an observed supercell storm and to the prediction of a real case are then presented. In the last case, a long-lasting squall line developed and propagated across the eastern part of the United States following a history number of tornado outbreak in the state of Arkansas.

Section 2 describes the land-surface soil-vegetation model and the treatment of surface-layer fluxes. Section 3 presents the microphysics and cumulus parameterization schemes used in the model, which is followed by a brief description of radiation parameterization schemes in Sect. 4. In Sect. 5, the parameterization of the PBL and surface layer, the soil model, and the radiation package are tested in a coupled mode to simulate the development and evolution of the PBL over a 48-hour period. In Sect. 6, the model is used to simulate a 3-D supercell storm using the sounding from the May 20, 1977 Del City, Oklahoma case (Ray et al., 1981). This particular set of experiments examines the model's ability to capture observed supercell storm characteristics in a classic cloud model setting. Additional insights are given on the effects of ice microphysics and/or advection schemes on the storm morphology and the amount of total precipitation from the storm.

In Sect. 7, the ARPS system, including the ARPS Data Analysis System (ADAS), is applied to the 48-hour prediction of a case involving an outbreak of 56 tornadoes and the development and evolution of a long-lasting squall line. Results from 32-km and 6-km resolution grids will be shown and compared with analyses and observations. This application demonstrates the full capabilities of the ARPS. Results from several

other validation experiments that are routinely performed on versions of ARPS are summarized in Sect. 8. An overall summary is given in the concluding section.

2. The land-surface and surface-layer processes

2.1. The land-surface soil-vegetation model

The state of the land surface has a direct impact on the sensible and latent heat exchange with the atmosphere, as the soil surface temperature and moisture content directly appear in the surface flux calculations (see Sect. 2.2 below). In the ARPS, the time-dependent state of the land surface is predicted by the surface energy and moisture budget equations, based on Noilhan and Planton (1989, NP89 hereafter), Jacquemin and Noilhan (1990), Pleim and Xiu (1995), and Boone et al. (1999). The heat energy budget includes net radiation, sensible heat fluxes, and ground heat flux into the ground. The surface moisture budget includes precipitation and dew formation, direction evaporation from the ground and vegetation canopy, evapotranspiration, runoff, and surface turbulent moisture flux. The model requires the definition of surface characteristics including soil and vegetation types, fractional coverage of vegetation (*veg*) and leaf area index (LAI). The information on vegetation is derived from normalized difference vegetation index (NDVI) according to satellite observations.

a. The soil-vegetation model

There are five prognostic equations in the soil model:

$$\partial T_s / \partial t = C_T (R_n \downarrow - H \uparrow - L \uparrow) - 2\pi(T_s - T_2)\tau^{-1}, \quad (1.1)$$

$$\partial T_2 / \partial t = -(T_2 - T_s)\tau^{-1}, \quad (1.2)$$

$$\begin{aligned} \partial W_g / \partial t = & C_1(P_g - E_g)(\rho_w d_1)^{-1} \\ & - C_2(W_g - W_{geq})\tau^{-1} - R_g, \\ 0 \leq W_g \leq W_{sat} \end{aligned} \quad (1.3)$$

$$\begin{aligned} \partial W_2 / \partial t = & (P_g - E_g - E_{tr})(\rho_w d_2)^{-1} \\ & - C_3 \max(0, W_2 - W_{fc})\tau^{-1} - R_2, \\ 0 \leq W_2 \leq W_{sat} \end{aligned} \quad (1.4)$$

$$\partial W_v / \partial t = \text{veg} P - E_v - R_v, \quad 0 \leq W_v \leq W_{v \max}. \quad (1.5)$$

Equations (1.1–2) are based on the force-restore models of NP89. The temperature (T_s) of a thin layer of depth d_1 (typically 1 cm) and the mean temperature (T_2) of the deeper soil layer (d_2) are predicted. The deeper layer acts as a slowly varying temperature reservoir. Here $R_n \downarrow$ is net radiation flux, $H \uparrow$ sensible heat flux and $L \uparrow$ latent heat flux. The net flux forces the diurnal change in T_s . The ground heat flux term, i.e., the second term on the RHS of Eq. (1.1) tends to restore T_s to the mean soil temperature T_2 of the deep layer. In Eq. (1.1), C_T is the inverse of the bulk heat capacity of the surface layer soil and vegetation [$C_T^{-1} = (1 - \text{veg})C_G^{-1} + \text{veg}C_V^{-1}$, where C_G is for soil and C_V for vegetation], and the soil portion is a function of deep layer volumetric soil moisture content, W_2 , and the soil type. As water content increases, C_T decreases so that the surface temperature rises more slowly.

Equations (1.3–4) describes the time rate of change in the volumetric soil moisture of the top layer (d_1) and in the average volumetric soil moisture of the deep layer of depth d_2 . P_g is the flux of liquid water reaching the soil surface, E_g the evaporation at the soil surface, E_{tr} the transpiration rate, and ρ_w the density of liquid water. W_{geq} is the W_g when gravity balances the capillarity forces, and R_g and R_2 represent runoff which happens when the respective water content reaches the saturation value (W_{sat}). C_1 , and C_2 are coefficients calibrated for each soil type according to NP89. The term with coefficient C_3 in Eq. (1.4) represents drainage from the bottom of the deep soil layer, and is based on Mahfouf et al. (1984). These equations show that the water content in each layer is forced by its respective net water fluxes, restored toward an equilibrium value in the surface layer, and is drained away when it is over a critical value (W_{fc}).

Finally, Eq. (1.5) describes the change in the canopy water content (depth) W_v , in response to P the precipitation rate, E_v , the evaporation rate (or dew flux when negative), and R_v , the runoff from the canopy water reservoir.

b. Net radiation flux

For surface heat balance, net radiative flux in (1.1) is given by

$$R_n = R_{sw}(1 - \alpha_g) + \varepsilon_g(R_A - \sigma T_s^4), \quad (2)$$

where R_{sw} is the shortwave radiation and R_A the atmospheric longwave radiation reaching the ground. Here α_g is the albedo and ε the emissivity combining the effect of soil and vegetation fractions. The σT_s^4 term is the emitted longwave radiation from the Earth's surface and σ the Stefan-Boltzman constant. The albedo is also dependent on W_g and the solar zenith angle.

c. Sensible and latent heat fluxes

The sensible heat flux in Eq. (1.1) is parameterized as

$$H \uparrow = \bar{\rho} C_{dh} C_p V (T - T_s), \quad (3)$$

where C_{dh} is the stability-dependent heat exchange coefficient which will be discussed in more details later. Here T is the air temperature taken at the first model level above ground and C_p is the specific heat at constant pressure for dry air.

The latent heat flux $L \uparrow$ is the sum of the evaporation from the soil surface (E_g), wet parts of the canopy (E_v), and evapotranspiration (E_{tr}):

$$L \uparrow = L(E_g + E_v + E_{tr}), \quad (4)$$

where L is the latent heat of evaporation.

The moisture flux from the bare soil portion of ground is given by

$$E_g = (1 - \text{veg}) \rho C_{dh} V [h_u q_{vsat}(T_s) - q_v], \quad (5)$$

where $q_{vsat}(T_s)$ is the saturation water vapor mixing ratio at ground temperature and h_u is ground surface relative humidity which is defined as a function of W_g according to NP89. q_v is the water vapor mixing ratio taken at the first model level above ground.

The fluxes from evapotranspiration and canopy water evaporation are, respectively:

$$E_{tr} = \text{veg} \rho (1 - F_w) [q_{vsat}(T_s) - q_v] (R_a + R_s)^{-1}, \quad (6)$$

and

$$E_v = \text{veg} \rho F_w [q_{vsat}(T_s) - q_v] R_a^{-1}, \quad (7)$$

where the wet fraction of the canopy $F_w = (W_v/W_{vmax})^{2/3}$. The aerodynamic resistance is parameterized as $R_a = (C_{dq} V)^{-1}$. The formulation for surface resistance, R_s , is more complicated and can be found in NP89.

d. Surface characteristics data base

For the ARPS, a data base of 13 soil types and 14 vegetation types are defined, with resolutions up to 1 km. The soil type data originated from the State Soil Geographic (STATSGO) data base (NSSC, 1994). The vegetation type data are taken from the world ecosystem classes data (Kineman and Ohrenschall, 1992). The leaf area index (LAI) and fractional coverage of vegetation (*veg*) are derived from the vegetation type and Normalized Difference Vegetation Index (NDVI) according to NOAA satellite observations (Kidwell, 1990). The roughness length is assigned according to vegetation type (Oke, 1978).

The availability of high-resolution soil and vegetation data set enables us to define multiple soil types in each ARPS model grid cell, with each type carrying a percentage weighting. The soil model and fluxes can be calculated once for each of these types and the weighted average of the fluxes is then passed to the atmosphere.

2.2. The surface layer physics

The atmosphere interacts with the underlying earth surface by exchanging momentum, heat and moisture. For the atmospheric model, this amounts to providing the lower boundary conditions for the momentum stresses (fluxes) τ_{13} and τ_{23} in Eq. (13) and the heat and moisture fluxes H_3 in Eq. (16), both in Part I.

a. Surface fluxes

The surface turbulent momentum fluxes are calculated by

$$\tau_{13}|_{surface} \equiv -[\rho \overline{u''w''}]_{surface} = \rho C_{dm} V u, \quad (8)$$

$$\tau_{23}|_{surface} \equiv -[\rho \overline{v''w''}]_{surface} = \rho C_{dm} V v, \quad (9)$$

where C_{dm} is the drag coefficient. u and v are evaluated at the lowest grid level above the ground and V is wind speed at the same level. In the code, a lower limit of 0.1 m s^{-1} is imposed on V to ensure nonzero fluxes under calm conditions. The double prime represents turbulent perturbation.

The surface sensible heat flux, $H \uparrow$, is given by Eq. (3). The heat flux, H_3 in Eq. (17) of Part I, for θ is then given by

$$H_3|_{surface} = H \uparrow \Pi C_p^{-1}. \quad (10)$$

The latent heat flux, $L \uparrow$, is given by Eq. (4). The surface moisture flux for q_v in Eq. (17) in Part I is therefore

$$H_3|_{surface} = L \uparrow L^{-1}. \quad (11)$$

b. Parameterization of drag coefficients

The coefficients C_{dm} , C_{dh} and C_{dq} in the flux formulations are functions of the stability and roughness length. One of the practical stability parameters is the bulk Richardson number:

$$Ri_b = g \Delta \theta (z - z_0) (\theta_0 U^2)^{-1}, \quad (12)$$

where z is the height of the surface layer, z_0 is the surface roughness length, $\Delta \theta = \theta_1 - \theta_s$, and θ_0 , θ_s and θ_1 are the base-state, surface and first-model-level potential temperatures, respectively. The environment is unstable if $Ri_b < 0$, neutral if $Ri_b = 0$, and stable if $Ri_b > 0$.

Let θ_* be the temperature scale representing the surface heat flux $w'\theta'_s$ divided by the frictional velocity u_* . According to the Monin-Obukhov (Monin and Obukhov, 1954) similarity theory,

$$u_* = C_u U, \text{ with } C_u = k [\ln(z/z_0) - \Psi_m(z/L, z_0/L)]^{-1}, \quad (13)$$

$$\theta_* = C_\theta \Delta \theta, \text{ with } C_\theta = k [Pr_0 \{\ln(z/z_0) - \Psi_h(z/L, z_0/L)\}]^{-1}, \quad (14)$$

where k is the von Karman constant, and Pr_0 is the Prandtl number.

We note the following relationships for the drag and exchange coefficients:

$$C_{dm} = C_u^2 = u_*^2 U^{-2} \quad (15)$$

and

$$C_{dh} = C_\theta C_u = u_* \theta_* (U \Delta \theta)^{-1}. \quad (16)$$

To obtain C_{dm} and C_{dh} , our next task is to compute C_u and C_θ . We define the functional form of Ψ_m and Ψ_h that depends on the stability as follows.

1) Unstable condition

For unstable conditions, we have (Byun, 1990)

$$\begin{aligned} \Psi_m = & 2 \ln[(1 + \chi)(1 + \chi_0)^{-1}] \\ & + \ln[(1 + \chi^2)(1 + \chi_0^2)^{-1}] \\ & - 2 \tan^{-1} \chi + 2 \tan^{-1} \chi_0, \end{aligned} \quad (17)$$

and

$$\Psi_h = 2 \ln[(1 + \eta)(1 + \eta_0)^{-1}]. \quad (18)$$

For a given Ri_b , ζ , Ψ_m , Ψ_h , C_u and C_θ can be computed from the above formulations.

2) Neutral condition

For the case of neutral stability, $(C_u)_{\text{neu}}$ and $(C_\theta)_{\text{neu}}$ are calculated using an extremely small negative Ri_b value, requiring the use of the equations for the unstable case given above.

3) Other conditions

For free convection or stable cases, C_u and C_θ are computed according to Deardorff (1972). Over the ocean surface, the surface roughness lengths are related to the surface wind speed. The momentum and thermal roughness lengths are computed based on Anderson (1993).

3. Precipitation processes

The precipitation in a numerical model is often divided into the grid scale and parameterized convective precipitation. For the former, the precipitation is produced by vertical circulation that is explicitly resolved by the grid. Even so, the microphysical processes that are responsible for the conversions among the microphysical species still have to be parameterized. In the case of parameterized precipitation, the entire process is parameterized and the procedures to achieve it are commonly referred to as cumulus parameterizations.

3.1. Microphysics parameterization

The ARPS includes the Kessler (1969) two-category liquid water (warm-rain) scheme and the modified three-category ice scheme of Lin et al. (1983). The implementation of the Lin et al. scheme follows that of Tao and Simpson (1993) and includes the ice-water saturation adjustment procedure of Tao et al. (1989). A simplified ice parameterization scheme of Schultz (1995) is also available as an option in ARPS, and it is attractive mainly due to its computational efficiency.

a. Kessler scheme

The Kessler warm rain microphysics parameterization includes three categories of water: water

vapor, cloud water and rain water. The Marshall-Pamler droplet distribution (Marshall and Palmer, 1948) is assumed for the cloud and rainwater. Saturation adjustment, autoconvection of cloud droplets to rain drops, accretion of cloud droplets by raindrops and rainwater evaporation are modeled. The sedimentation of rain drops is parameterized. Our implementation of this scheme follows Klemp and Wilhelmson (1978), and Soong and Ogura (1973).

b. Ice microphysics

One ice microphysics scheme in the ARPS includes two liquid phases (cloud and rain) and three ice categories (ice cloud, snow and hail or graupel) after Lin et al. (1983). The scheme assumes that the particle size distribution functions for rain, snow, and hail/graupel have an exponential form and all ice particles are spherical in shape.

The source terms denoted by S_q in the conservation equation (8.6) in Part I for cloud water (q_c), rain (q_r), cloud ice (q_i), snow (q_s) and hail/graupel (q_h) include the following conversion terms:

$$S_{q_c} = \rho(c - e_c) - T_{q_c}, \quad (19.1)$$

$$S_{q_r} = \rho(-e_r + m_s + m_h - f_s - f_h) - T_{q_r}, \quad (19.2)$$

$$S_{q_i} = \rho(d_i - s_i) - T_{q_i}, \quad (19.3)$$

$$S_{q_s} = \rho(d_s - s_s - m_s + f_s) - T_{q_s}, \quad (19.4)$$

$$S_{q_h} = \rho(d_h - s_h - m_h + f_h) - T_{q_h}. \quad (19.5)$$

The symbols c , e , f , m , d and s stand for the rates of condensation, evaporation of droplets, freezing of raindrops, melting of snow and graupel, deposition of ice particles, and sublimation of ice particles, respectively. The terms T_{q_c} , T_{q_r} , T_{q_i} , T_{q_s} and T_{q_h} are microphysical transfer rates between the hydrometeor species pairs, and their sum is zero. The complicated transfers encompass nearly thirty processes. They include autoconversion that parameterizes the collision-coalescence and collision-aggregation, accretion that involves the various forms of liquid and solid hydrometeors. The transformation of cloud ice to snow through autoconversion (aggregation) and Bergeron processes (Bergeron, 1935) and subsequent accretional growth or aggregation to form hail are simulated. Hail is also produced by various contact mechanisms and via probabilistic freezing

of raindrops. Evaporation (sublimation) is considered for all precipitation particles outside the cloud. The melting of hail and snow, wet and dry growth of hail and shedding of rain from hail are included. The actual formulation of each of the transfers can be found in Lin et al. (1983).

For the saturation adjustment processes, a relaxation technique is used to iteratively balance the heat exchange and change of phase of water substance (Tao et al., 1989). Initiation of cloud ice and depositional growth of cloud ice discussed in Rutledge and Hobbs (1984) is used to initiate the cloud ice in a saturated environment. This procedure weighs the saturation mixing ratio in favor of ice at levels above the freezing level 0°C . This adjustment scheme will almost guarantee that the cloudy region (area containing cloud water and/or cloud ice) is always saturated (100% relative humidity). This permits subsaturated downdrafts with rain and hail/graupel particles but not cloud-sized particles.

3.2 *Cumulus parameterization*

For grid resolutions incapable of explicitly resolving convective circulations, parameterization of cumulus convection is necessary. The ARPS includes the Kuo (1965; 1974) and Kain-Fritsch (1990; 1993) parameterization schemes. The former was designed for grid spacings on the order of 50 km or greater and the latter is more suitable for higher resolution grids. A critical review of the Kuo scheme can be found in Raymond and Emanuel (1993).

In the ARPS, the cumulus parameterization can be used in combination with the microphysics options. Further, the Kain-Fritsch scheme can generate sources of rainwater and snow that are fed back to the grid scale variables which then interact with the ice microphysics processes. The heat, moisture and hydrometeor sources from the parameterization appear on the RHS of equations (8.5-6) and are generally updated for periods of time comparable with cloud life cycle. The cumulus parameterization uses vertical velocity, w , as part of the decision to activate (trigger) cumulus rainfall. To reduce the chances of short impulses in the low-level w triggering (parameterized) convection, a running mean in time is applied to the w fields before they are used in the trigger function.

4. Parameterization of radiation processes

The radiation plays an important role in NWP. It is the primary forcing for the soil model in terms of the surface energy budget. Radiation-cloud interaction is equally important. A sophisticated long- and short-wave radiation package developed at the NASA/Goddard Space Flight Center has been adapted for use in the ARPS. Within this package, the shortwave radiation is based on the models of Chou (1990; 1992) which calculates solar heating in the atmosphere and at the earth's surface. The solar spectrum is divided into the ultraviolet and visible regions in which ozone absorption, Rayleigh and cloud scattering are included. The long-wave radiation model is based on Chou and Suarez (1994), and calculates cloud and atmospheric infrared cooling. The scheme had been adapted for use in a cloud ensemble model (Tao et al., 1996).

5. Validation of soil-vegetation, surface physics and PBL

As described earlier, the land surface and vegetation model in the ARPS follows Noilhan and Planton (1989), and Pleim and Xiu (1995). The net radiation reaching the ground is modeled by the Chou (1990; 1992), and Chou and Suarez (1994) radiation parameterization. The planetary boundary layer (PBL) parameterization is a combination of the 3-D, 1.5-order Deardorff (1980) type subgrid scale (SGS) turbulence scheme and a 1-D ensemble turbulence closure scheme of Sun and Chang (1986). In this section, the coupled soil-vegetation model, surface layer, PBL and radiation parameterizations are verified in 1-D against data from Day 33 of the Wangara boundary-layer field experiment (Clarke et al., 1971). Earlier 1-D and 3-D results of PBL development forced by observed surface fluxes were reported in Xue et al. (1996).

5.1. *The Experiment*

The model is initialized using a 9 EST (Eastern Standard Time in Australia) sounding of Day 33 taken at Hay, Australia during the Wangara experiment. Unlike Xue et al. (1996) and work by Sun and Chang (1986) and some others, the surface momentum, heat and moisture fluxes are

calculated by the surface layer model with stability-dependent drag coefficients and land surface conditions predicted by the soil model. Large-scale geostrophic and thermal winds linearly interpolated between the observation times and heights are used. A vertical grid spacing of 50 m is used with a total of 230 layers. Time step size is 60 s for both atmospheric and the soil models. For the soil model, soil type used is loam, vegetation type is desert, leaf area index is 0.1, vegetation fraction is 0.05 and roughness length is 0.24 m. Initial ground wetness (volumetric water content) is 0.1533 and that of the deep layer is 0.1555.

5.2. The results

The vertical profiles of simulated and observed virtual potential temperature (θ_v) and specific humidity (q_v) at various times are plotted in Fig. 1. Figure 1a shows that a mixed boundary layer is fully developed by 15 EST. A shallow superadiabatic layer near the surface and a layer at the boundary layer top with negative θ_v perturbations resulting from entrainment are seen. Both features are observed, although the model PBL is slightly deeper than the observation. By 18 EST, radiative cooling dominates at the surface and θ_v drops 282.7 K as compared to the observed

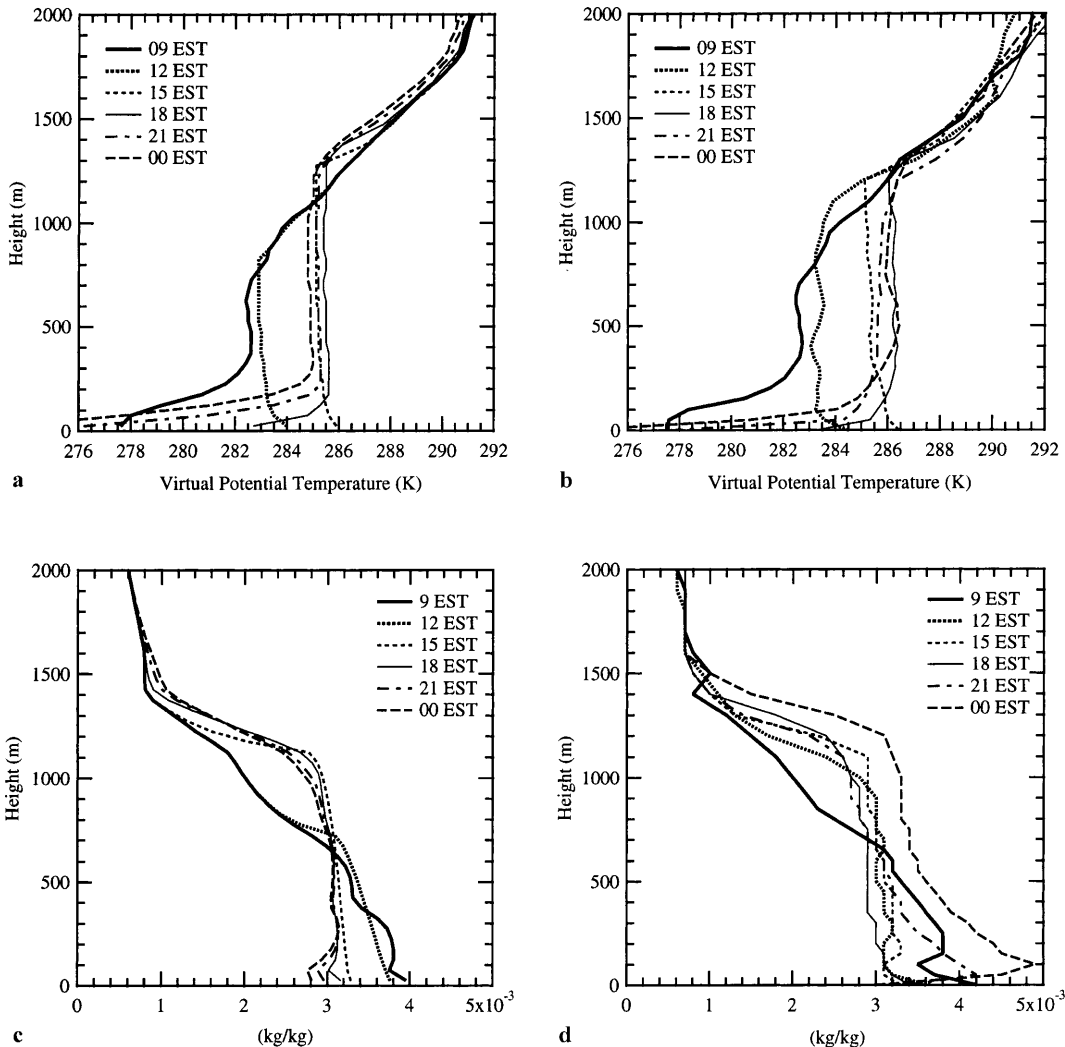


Fig. 1. Profiles of virtual potential temperature, θ_v , (upper panel) and specific humidity, q_v , (lower panel) simulated by ARPS (left panel) and from Wangara Day 33 data (right panel)

283.4 K. Surface cooling continued into the night and deepens the stable boundary layer to about 200 m depth, which is somewhat deeper than the observed one. The simulated vertical temperature *fluxes* decrease linearly with height and become negative in the entrainment layer, similar to the observations (not shown).

The vertical mixing dries the surface layer and moistens in the upper PBL (Fig. 1c) in the model, again agreeing with the observation (Fig. 1d). Overall, the evolution of the simulated PBL agrees remarkably well with the observations (Clarke

et al., 1971) as well as these obtained from a high (third) order turbulence model of André et al. (1978).

The performance of the radiation parameterization and the soil model can be illustrated by comparing ground surface radiation, heat and moisture fluxes with observations. Figure 2 shows that, for a 48-hour period, the model produces well-behaved diurnal cycles in the fluxes. The magnitude and phase of the net radiation, heat and ground fluxes all agree well with observations. The latent heat flux is relative small in such a dry condition.

The results from the above experiment, and the comparison with the First International Satellite Land Surface Climatology Project (ISLSCP) Field Experiment (FIFE, Sellers et al., 1992) data (Xue et al., 1995) and with HAPEX-MOBILHY (André et al., 1986) data (not shown) provide reasonable validations for our coupled soil – atmosphere model, at least for the specific geophysical and weather conditions. More detailed studies using Oklahoma Mesonet (Brock et al., 1995) measurements are being carried out that will test more diverse conditions.

6. May 20, 1977 Del City supercell storm simulation

The 20 May 1977 Del City, Oklahoma storm is a well-documented and extensively studied tornadic supercell storm. The morphology and evolution of this storm was documented in Ray et al. (1981) based on multi-Doppler radar analysis. Early numerical simulations by Klemp et al. (1981) simulated the general supercell morphology reasonably well, even though the storm was started from artificial initial perturbations in a horizontally homogeneous environment. Later, a high-resolution study by Klemp and Rotunno (1983) using the same sounding was able to simulate tornadic vortex intensification near the tip of a surface gust front occlusion. More recently, this storm was simulated by Lin et al. (1993) using inhomogeneous initial conditions derived from multiple Doppler radars, and by Xue et al. (1993) at high resolutions using the adaptive grid refinement technique in the ARPS. These studies all used Kessler-type (Kessler, 1969) warm rain microphysics, however. In this section, we present the results from the ARPS, using the same

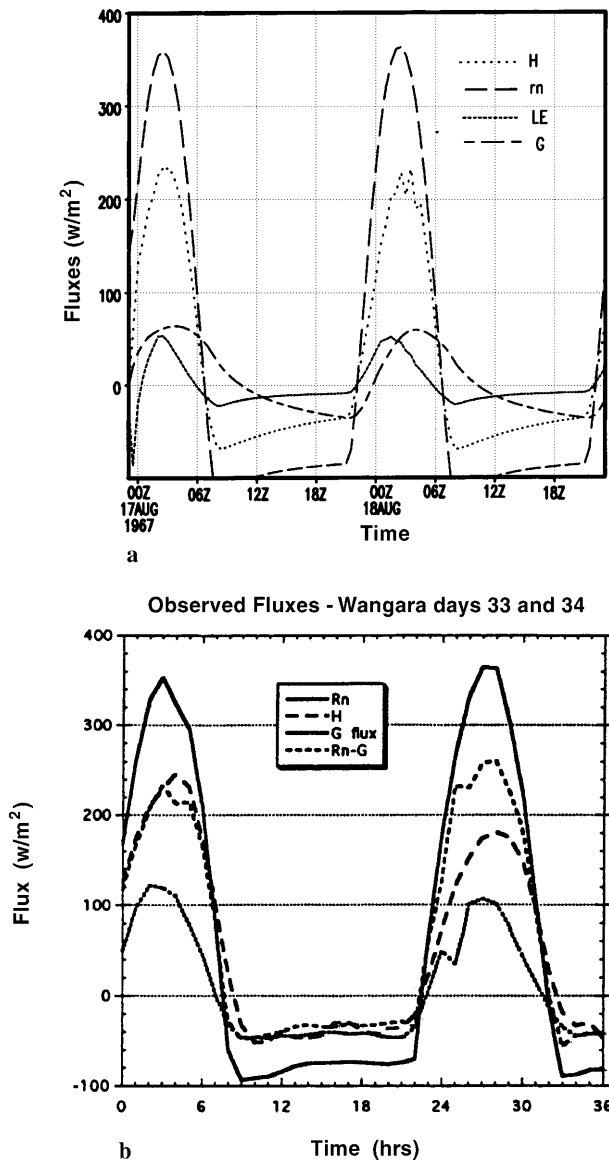


Fig. 2. The simulated **a** and observed **b** surface fluxes of net radiation (R_n), sensible heat (H), latent heat (LE), and ground heat (G) for Wangara days 33 and 34. 0Z corresponds to 9 am local time

initial sounding as in Klemp et al. (1981), and compare the results against the observations and the simulation of Klemp and Wilhelmson (1978). We also examine the impact of monotonic and positive definite advection schemes and the ice microphysics on the intensity and precipitation amount of the storm. These experiments also demonstrate the model's ability to simulate intensive convective systems.

6.1. The experiments

For all experiments, the horizontal grid spacing is 1 km and the vertical grid is stretched from 100 m at the ground to 700 m at the top. The domain is $64 \times 64 \times 16 \text{ km}^3$ in size. The storm was initiated by a 4°C ellipsoidal thermal bubble centered at $x = 48 \text{ km}$, $y = 16 \text{ km}$ and $z = 1.5 \text{ km}$, and with radii of 10 km in x and y directions and 1.5 km in the vertical direction. The Orlanski (1976) open lateral boundary condition but with the column averaged phase speed estimation as proposed by Durran and Klemp (1983) (option 4 in ARPS) is used. A radiation condition is also used at the top boundary. A cosine instead of regular Fourier transform is used in the condition which removes the constraint of lateral periodicity (see Part I).

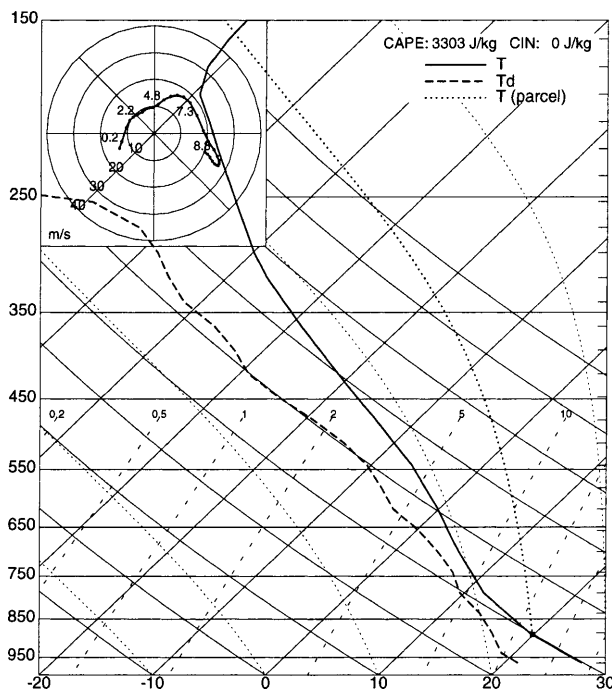


Fig. 3. Sounding used for the Del City storm simulation. It is a smoothed version of that used in Klemp et al. (1981)

The 1.5-order turbulent kinetic energy (TKE)-based subgrid-scale (SGS) turbulence option is used whose implementation follows Moeng (1984). Free-slip conditions were applied to the bottom boundary. The large and small time step sizes are 3 s and 1 s, respectively. The storm environment is defined by a sounding shown in Fig. 3. A constant wind of $u = 3 \text{ ms}^{-1}$ and $v = 14 \text{ ms}^{-1}$ is subtracted from the original sounding to keep the primary storm cell near the center of model grid. Fourth-order computational mixing is applied in both horizontal and vertical directions.

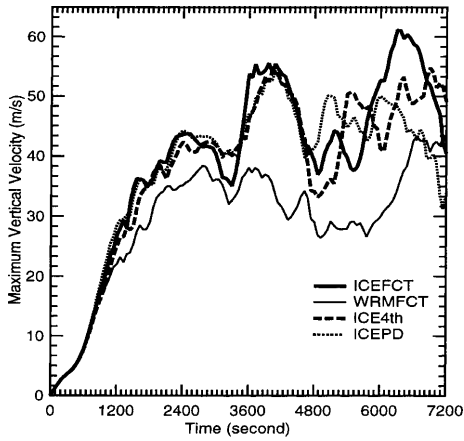
The results from four experiments are presented (see Table 1). They differ in their use of advection schemes for temperature, water species and TKE and in the choice of microphysics parameterization. In all cases, the momentum fields are advected by fourth-order leapfrog centered scheme. When this scheme is used (in ICE4th) to advect positive definite fields (water species and TKE), negative values are set to zero which constitutes a source of error. The implementation of the monotonic FCT (flux-corrected transport) scheme follows Zalesak (1979), with modifications so that extrema in the advected scalar instead of density-weighted scalar is used in the flux limiting process. The high-order scheme used is a second-order-in-time, fourth-order-in-space trapezoidal scheme while the lower-order scheme is upstream in space and forward in time. This option was used in the density current experiments in Part I. Experiment ICEPD uses the positive definite scheme of Lafore et al. (1998) for the advection of water, ice and TKE fields. This scheme limits the outgoing fluxes (only) in each grid volume using a limiter after Zalesak (1979) so that the advected positive fields do not go negative.

6.2. The results

The general strengths of the simulated storms (c.f. Table 1) are measured by the time series of the maximum vertical velocity (w) in Fig. 4. It can be seen that the maximum vertical updraft first reaches a peak of 44 ms^{-1} at 40 minutes, then decreases by 5 to 10 ms^{-1} until it reaches another maximum after 60 minutes. This first weakening of updraft is associated with the splitting of the initial cell into two (c.f. Fig. 5), with a tendency

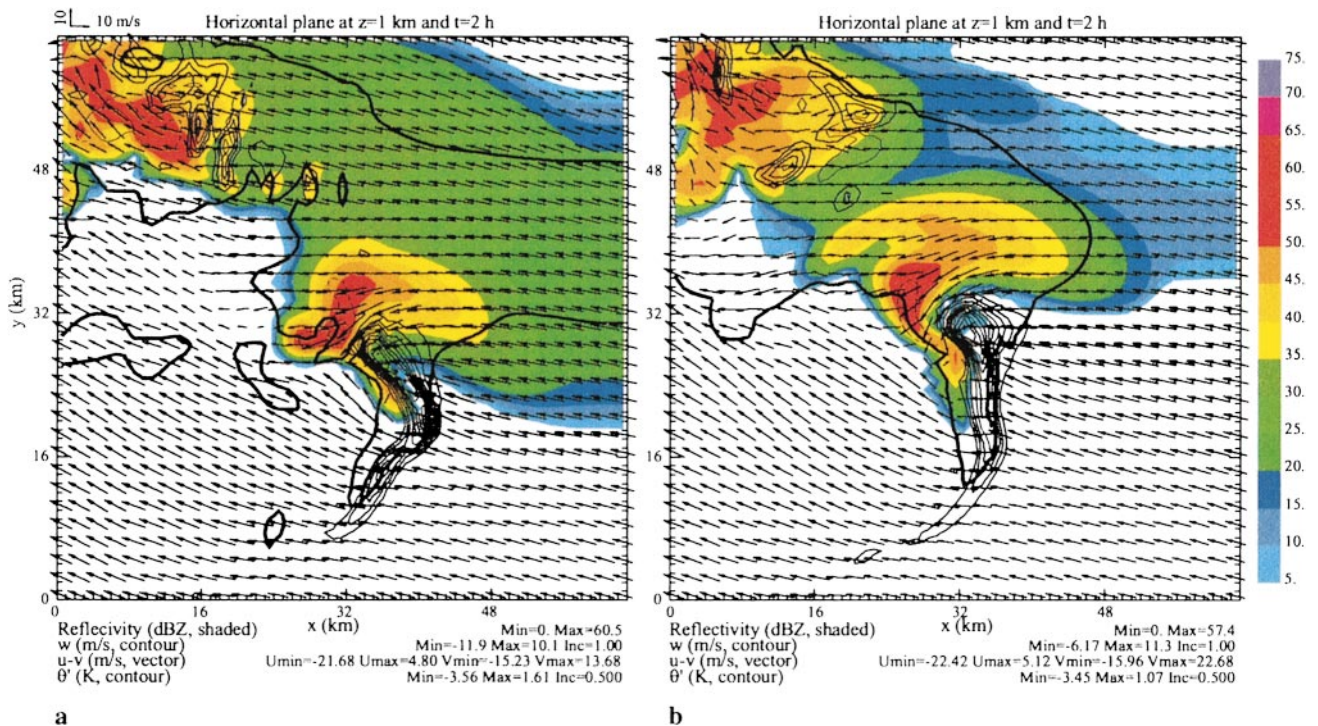
Table 1. List of May 20, 1977 supercell storm simulations

Experiment	Advection	Microphysics
ICEFCT	FCT	Ice
ICE4th	4th-order centered	Ice
ICEPD	Positive-definite 4th-order centered for positive fields	Ice
WRMFCT	FCT	Kessler warm-rain

**Fig. 4.** The time series of the maximum vertical velocity (representing updraft strength) in four simulations of May 20, 1977 Del City OK supercell storm (see Table 1)

for the right mover to dominate the system. Three tests with ice microphysics exhibit similar maximum vertical velocities (about 55 ms^{-1} around 65 min), with significant differences not appearing until after 80 min. The updrafts in the warm-rain run, without the help of extra heating of freezing, are much weaker. The peak w remains under 40 ms^{-1} most of the time. The updraft in ICEFCT run reached greatest strength among all, with maximum w reaching 60 ms^{-1} after 100 min. This can be attributed to the better conservation of equivalent potential temperature in the parcels that are advected by the monotonic FCT scheme.

The horizontal cross-sections at 1 km height from simulations ICEFCT and WRMFCT are shown in Fig. 5. In both cases, at the center of domain is the right mover formed from earlier splitting. Strong vertical rotation is clearly depicted by wind vectors and by the hook-shaped reflectivity (radar echo) fields wrapping around the main updraft. The low-level cold pool is indicated by the $-0.5 \text{ K } \theta'$ contours. The updraft is found along the boundary of the forward flank outflow while the downdraft is strongest underneath the heavy precipitation areas, as indicated by the high reflectivity. The shape of the echo in

**Fig. 5.** Horizontal wind vectors, vertical velocity (thin contours at 1 m s^{-1} intervals), outline of cold pool front (represented by thick $\theta' = -0.5 \text{ K}$ contours), and simulated reflectivity field (color shaded), at $z = 1 \text{ km}$ and $t = 2 \text{ h}$, for experiments **a** ICEFCT, and **b** WRMFCT. The entire computational domain is shown

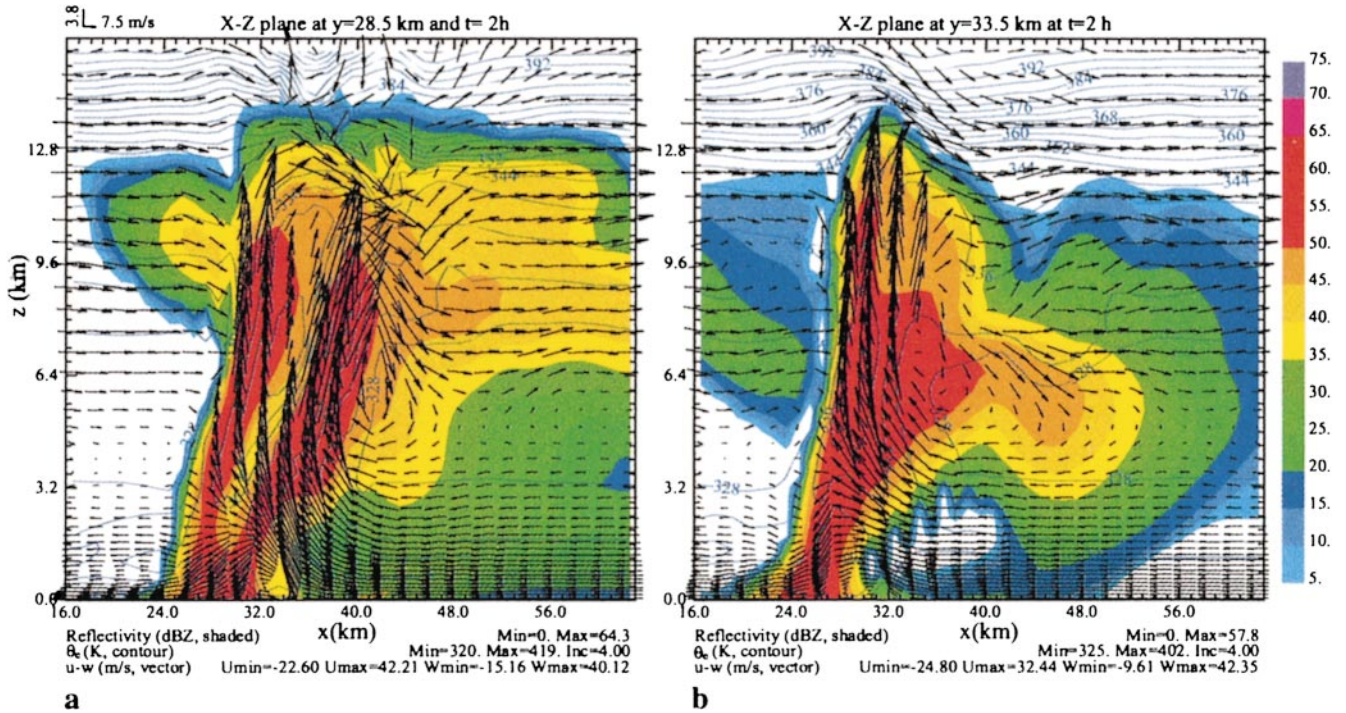


Fig. 6. X-Z vertical cross-sections through updraft cores of simulation **a** ICEFCT, and **b** WRMFCT. Shown in the figure are vertical wind vectors, equivalent potential temperature contours, and color shaded simulated reflectivity fields. Only a portion of the domain is shown

the warm-rain case is very similar to that of Klemp et al. (1981, Fig. 4a) who used similar microphysics, and it compares well with observations (Fig. 6a). The region of strong radar echoes in the ice test is smaller and is more tightly wrapped around the primary updraft core. The occlusion inside the hook region is apparently more fully developed. The regions of lighter precipitation are, on the other hand, much broader than the warm-rain case, indicating a more vigorous system with fully developed anvils. The more slowly falling ice particles also aided this development, while warm-rain microphysics typically under-predicts the formation of anvils. Arguably, the simulated flow and reflectivity patterns in the ice run agree with the observations better (c.f., Fig. 6a of Klemp et al., 1981).

The x - z vertical cross-sections through maximum w in the above two cases are shown in Fig. 6. It is clear that the ice case is more vigorous and the cloud anvil spreads over a wider area at upper levels. In these vertical cross sections, gravity waves forced by the overshooting cloud top at the tropopause level are evident, and these waves are allowed by the radiation condition to propagate through the upper boundary. The continuation of

the equivalent potential temperature (θ_e) contours through the updraft regions indicates good conservation of θ_e in the updraft parcels along their trajectories. The updrafts exhibit down-shear tilt in the cross-section, a structure sustainable only in three dimensions, where updrafts and downdrafts can be organized in a three-dimensional space to avoid down-loading rain-water directly onto the low-level inflow.

Further, we point out that the lateral boundaries, with the use of open boundary conditions, are well behaved, even though strong cells associated with the left mover as well as low-level outflow passed through the boundary (Fig. 5) during the 2 hour period. The pressure field is free of systematic drift, which often occurs in a compressible model with improperly implemented open boundary conditions. The pressure field near the lateral boundaries is clean.

Finally, we compare the 2-h accumulated precipitation fields and their domain averaged values produced by the above four simulations. Fig. 7 shows that the warm-rain microphysics produces the least amount of precipitation while experiment ICE4th produces the most amount. The latter may be surprising because the fourth-

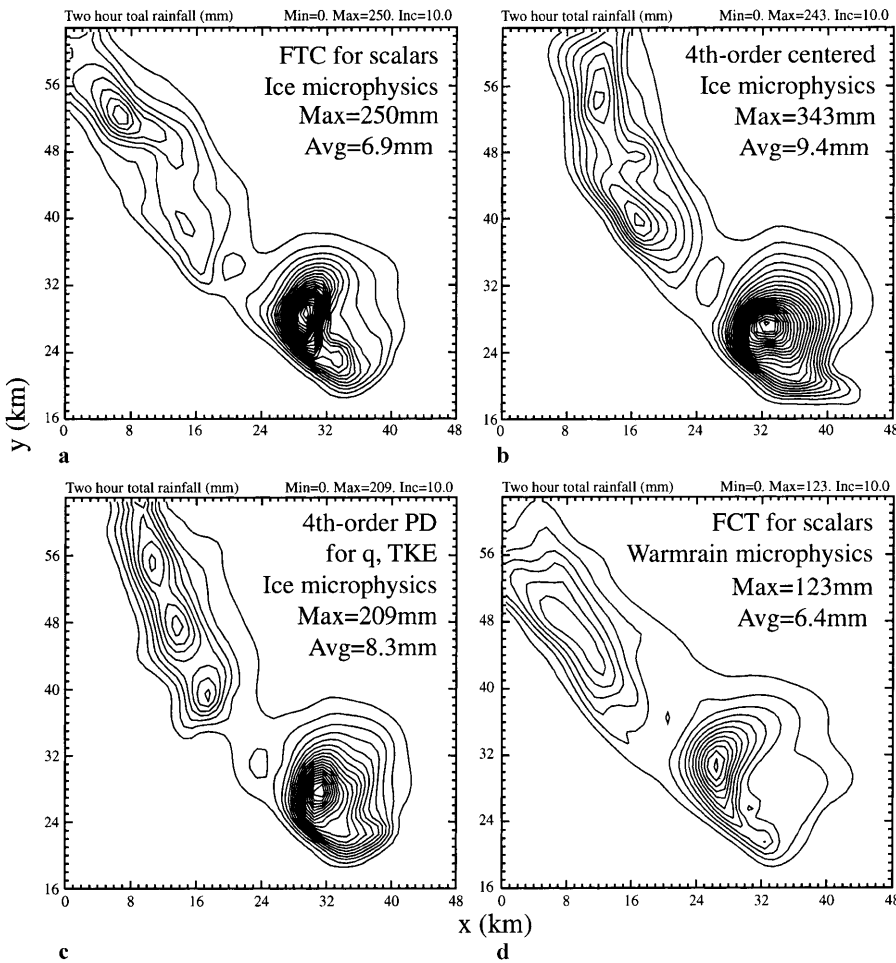


Fig. 7. Two hour accumulated precipitation from simulations of the May 20, 1977 Del City, OK supercell storm, using **a** FCT scalar advection and ice microphysics, **b** 4th-order centered advection and ice, **c** FCT and warm-rain microphysics, and **d** positive-definite 4th-order centered advection applied to water and TKE fields and warm-rain microphysics. The local maximum and domain average are shown in the plots

order centered advection is less conservative than the FCT scheme. This behavior is attributed to the presence of spurious water/ice sources when negative water/ice values produced by advection are set to zero. The error is particularly large at the transition zone near freezing level where sharp gradients exist in the water and ice fields. Applying a positive definite flux limiter to the scheme leads to a more reasonable result in ICEPD, in which the maximum local precipitation is reduced to below that of FCT run. The domain average is still higher, presumably due to the presence of overshooting in the advected fields. These results demonstrate the important impact of advection schemes on the forecast of precipitation in convective storms, and the significant differences resulting from varying the treatment of microphysical processes.

In summary, we presented in this section the results of simulations of a well-documented supercell storm, using three different advection options, two choices of microphysics parameterizations,

and open boundary conditions. The simulation with the monotonic FCT scheme and ice microphysics produced results most agreeable to the observations and our physical understanding. The results from the other runs are consistent with our expectations.

7. A real data prediction experiment

The ARPS is designed to be a tool for both research and numerical weather prediction. In this section, we present the results from a prediction experiment with a 6-km resolution grid nested within a continental-scale 32 km grid-spacing grid. The ARPS Data Analysis System (ADAS, Brewster, 1996) is used to produce the initial conditions and in the intermittent data assimilation cycle. The Arkansas (AR) tornado outbreak case of January 21, 1999 is chosen to illustrate the model's multi-scale capability.

A major tornado outbreak occurred from southwest into central and northeast Arkansas during

the afternoon and evening of January 21, 1999 (mostly between 4 pm and 8 pm CST, i.e., 22 UTC January 21 through 02 UTC January 22). Fifty-six tornadoes were produced statewide (the strongest tornadoes are rated at F3 on the Fujita Scale) and eight people were killed by the tornadoes. It is believed to be the largest tornado outbreak in Arkansas. The historical average number of tornadoes in the state is 21 per year. This case is even more unusual given that it occurred in January. In fact, it is a case of the most tornadoes in any state during January.

7.1. Case introduction

At 12 UTC (6am CST), January 21, the surface chart was dominated by a low-pressure system with two connected centers located at northeast

Colorado (CO) and western Oklahoma (OK), respectively (Fig. 8a). To the east of the OK low center, Arkansas was under the influence of strengthening low-level southerly flows originating from the Gulf of Mexico (Gulf hereafter). Above the 700 hPa level, a broad trough was located over the central US with a strong baroclinic zone stretching from northern California (CA) along the CA-Nevada (NV) border into Arizona (AZ). Overlaying this zone was a strong jet with a maximum speed of over 80 ms^{-1} at the 250 hPa level (Fig. 8a). During the next 12 hours, this trough deepened significantly on the leeside of the Rocky mountain range. A short-wave trough found over the Idaho and Wyoming border at 12 UTC (Fig. 8a) propagated eastward and merged with the major trough (Fig. 8b), apparently contributing to the deepening of the latter.

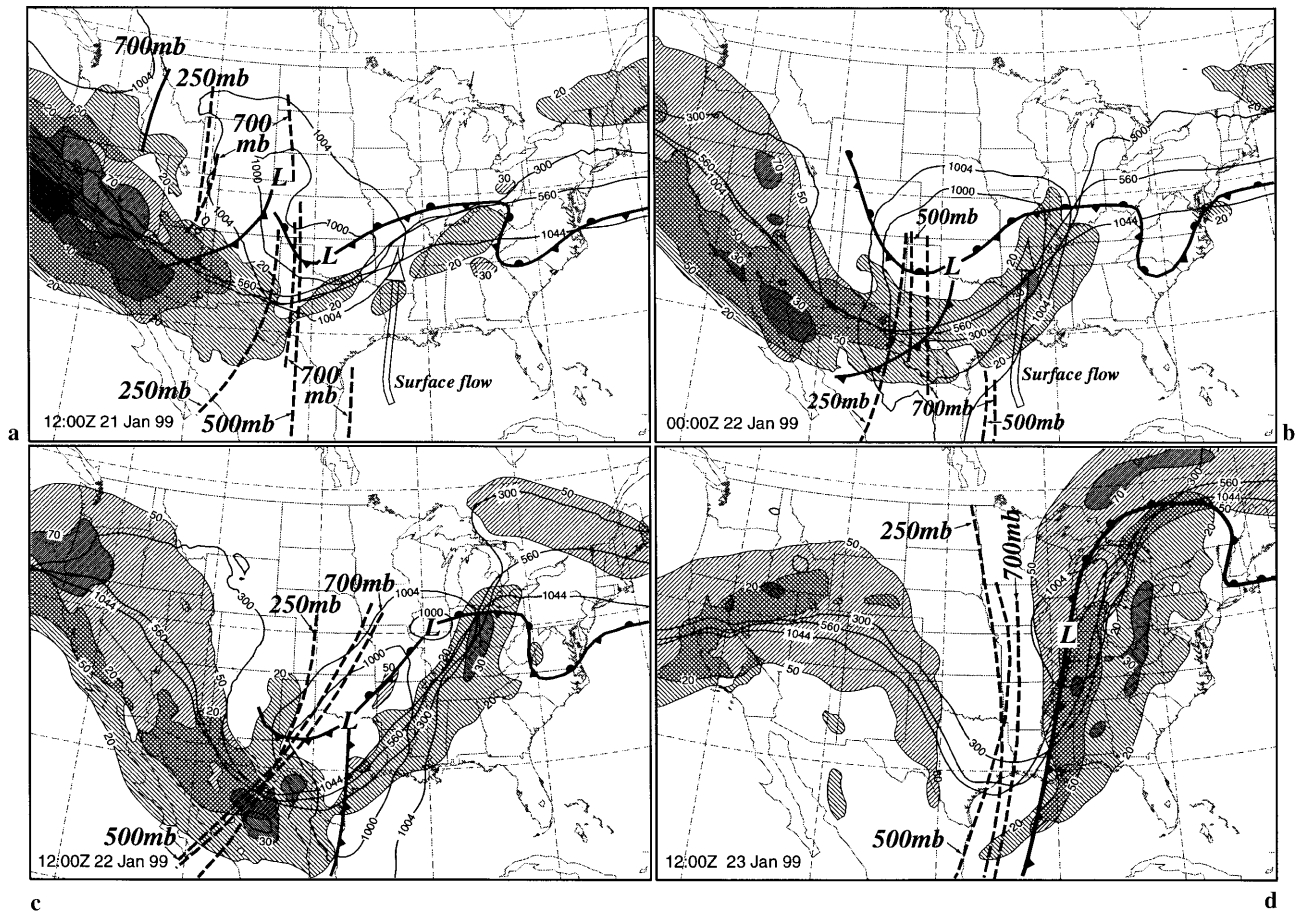


Fig. 8. Composite plots based on NCEP Eta analyses at **a** 12 UTC Jan 21, **b** 00 UTC Jan 22, **c** 12 UTC Jan 22, and **d** 12 UTC Jan 23, 1999. Shown in the plots are 700 hPa 300 decameter, 500 hPa 560 decameter and 250 hPa 1044 decameter geopotential height contours, 1000 and 1004 hPa mean sea-level pressure contours. 700 hPa 20 and 30 ms^{-1} isotachs are shown with negatively tilted thin and heavy hatching patterns, respectively, and 250 hPa 50 and 70 ms^{-1} isotachs with positively tilted thin and heavy hatching patterns, respectively. Trough axes at three pressure levels are shown as bold dashed lines and ridge axis in bold solid line. Surface fronts associated with the low-pressure system are also analyzed

The base of this major trough reached southwestern Texas (TX) at 00 UTC, January 22 while the trough axis remained more or less stationary (Fig. 8b). During this period, a baroclinic zone became well defined ahead of the trough, extending from SW TX through NW AR into Missouri (MO) (not shown). The jet at all levels propagated eastward relative to the trough axis. At 00 UTC, a local maximum of more than 30 ms^{-1} was found over SE AR at the 700 hPa level. At the 250 hPa level, the 50 ms^{-1} isotach reached the trough axis (Fig. 8b) while the leading edge of the jet extended much further. At this level, the central axis of the jet stream east of the trough axis was located along the east-west Gulf coast, placing AR on the left side of the upper-level jet-exit region, where the flow was evidently diffluent.

With the deepening of upper-level trough, two low centers found at 00 UTC (Fig. 8a) merged into a single one centered over SW OK and the central pressure dropped by about 6 hPa (Fig. 8b). The surface winds over Louisiana (LA) and AR became stronger, supplying warm and moist air into the SE portion of Arkansas. The surface-based convective available potential energy (CAPE) reached about 2000 J/kg south of a boundary stretching across the SE corner of OK and the NE corner of AR (not shown). The strong low-level southerly winds established a vertical shear that was favorable for supercell storms. The above conditions worked together to provide a favorable environment for supercell storms capable of spawning tornadoes. Indeed, during the four hour period surrounding 00 UTC of January 22, a series of supercell storms formed and moved northeastwards along a diagonal axis through SW and SE AR, coinciding with the NE boundary of the high CAPE region. These storms produced 56 tornadoes. It is noted here that these tornadic storms occurred in the warm sector of a surface cyclone, way ahead of a surface cold front located to the west.

After the tornado outbreak, the storm system continued to evolve and became more organized during the next 36 hours. From 00 UTC to 12 UTC, January 22, the 500 hPa trough deepened further by extending its base into SW TX and northern Mexico, and the trough axis gained a SW-NE orientation (Fig. 8c). A northeastward extending ridge is found to the northwest of the deep trough at the 700 hPa level. The Rocky Mountains must

have played an important role in the trough deepening and the ridge amplification as the jet stream passes over the Rockies. At the surface, the low-pressure system became elongated with one center located at the south-OK and north-TX border and the second center located over Indiana (IN) (Fig. 8c). The minimum sea-level pressure at the center was higher at 12 UTC, however.

After 12 UTC January 22, the 500 hPa trough started to move away from the eastern edge of the Rockies, with the trough axis reaching central-eastern OK and central TX by 00 UTC (not shown) then western AR and TX-LA border by 12 UTC, January 23 (Fig. 8d). The trough axis turned from a SW-NE orientation to a nearly N-S orientation. After 12 UTC January 22, the upper-level trough became narrower as it began to fill. The 500 hPa maximum jet core of about 50 ms^{-1} propagated from west of the trough axis over Northern Mexico at 12 UTC January 22 to east of the trough axis over AR and northern LA by 00 UTC then to NW Mississippi (MS) by 12 UTC January 23 (not shown). During the same period, the jets ahead of the trough axis at the 700 and 250 hPa levels also significantly strengthened and propagated northeastward. The 250 hPa jet is located on the left side of the 700 hPa jet. At the surface, the SW-NE oriented elongated surface low-pressure system turned into a nearly N-S orientation, with its northern part essentially anchored in Indiana (IN). The primary low center moved ENE to the AR-MS border by 00 UTC January 23 then NNE to NW IN by 12 UTC (Fig. 8d).

After the tornado outbreak, the most interesting weather is the formation of an intense squall line in the warm sector of the surface cyclone, ahead of a surface cold front (SCF). At the later time, this line extended from north of the low-pressure center in the Great Lakes region all the way into the Gulf.

According to radar observations (not shown, see also satellite images in Fig. 11), from 00 to 01 UTC January 22, a line of convective cells formed along the eastern border of LA and AR and the line remained stationary while individual cells moved northward along the line. During the next five hours, the north portion of this line merged with the tornado-spawning cells in the eastward moving, SW-NE oriented, line that was originally running through central AR. For the next two hours, the southern portion weakened until a

line originating from the SCF to the west overtook and merged with this line. At 9 UTC January 22, an almost continuous line was seen stretching from east-central TX, through NW LA, SE AR and northward along the Mississippi river. The southern portion moved eastward and underwent a reorganizing phase as new cells developed ahead and behind the line until, eventually, a single-line structure was established along the eastern border of LA by 20 UTC. The southern end of the line extended about 150 km offshore into the Gulf. After this time, this line, in particular its southern portion, started rapid eastward propagation. By 12 UTC, January 23, it had reached the Alabama (AL) and Georgia (GA) border and its southern end extended about 700 km offshore into the Gulf. In general, the precipitation in the southern portion of the line was mostly convective while that in the northern portion was mostly stratiform in nature.

7.2. ARPS forecast experiment

As described earlier, many processes at scales ranging from baroclinic waves down to tornadoes were present in the January 21–23, 1999 case. Interesting processes and features include large-scale flow-mountain interaction, upper and low-level jets, surface cyclones and fronts, squall lines, super-cell storms and tornadoes. There were also interactions across these scales. It is therefore a very good case for testing and demonstrating ARPS's capabilities as well as evaluating its performance.

Results from two computational grids will be shown; one has a 32-km and another a 6-km resolution in the Lambert projection plane. The $215 \times 155 \times 43$ 32-km grid covers the entire contiguous US and part of surrounding countries. This grid resolves the synoptic-scale flow and provides boundary conditions for the one-way nested 6-km grid. The 6-km grid is centered at the SW corner of the state of Illinois and covers a $2172 \times 2172 \text{ km}^2$ domain. This grid intends to resolve flows at the meso- and organized convection scales. An additional 2-km grid has been further nested within the 6 km, whose results will be discussed only briefly. The vertical grid intervals are increased from 20 m at the surface to nearly 1 km at the 20-km height using a formula based on a hyperbolic tangent function described in Xue et al. (1995).

For all simulations, 4th-order advection and computational mixing were used. The physics options include 1.5-order TKE-based SGS turbulence and PBL parameterization, two-layer soil model, explicit grid-scale ice microphysics (Tao-Lin option) and NASA/GSFC radiation physics (see Part I for more details on the options). The radiative forcing is updated every 10 minutes. For the soil model, three fractional subgrid soil types were defined for each grid cell to take advantage of the high-resolution database. The soil model is initialized using fields available in the Eta analyses from the National Center for Environmental Prediction (NCEP). The 32-km grid differs from the 6-km one in that the Kain-Fritsch cumulus parameterization scheme is used in combination with the explicit ice microphysics. At the lateral boundaries, a 5-cell wide relaxation zone is used for both grids. At the upper levels Rayleigh damping is applied. The 32-km simulations were performed on a Cray J90 in a shared-memory-parallel mode, while the 6- and 2-km runs were completed on a SGI Origin 2000 in distributed-memory-parallel mode using 128 or 256 processors.

For both grids, the model runs span a 48-hour period, starting from 12 UTC January 21, about 10 hours before the AR tornado outbreak, to 12 UTC January 23, when the mature squall line reached the eastern coastal states. The NCEP Eta analyses at 12 hour intervals interleaved with their respective 3-hourly forecasts were linearly interpolated in time and used to provide lateral boundary forcing for the 32-km grid. The 12 UTC NCEP Eta analysis was used as the first guess for the ADAS analyses on all grids. Rawinsonde, wind profiler, NWS surface and Oklahoma Mesonet data were used in the analysis. For the control simulation, a 24-hour hourly intermittent data assimilation cycle (using ADAS) is performed on the 32-km grid, starting from 12 UTC January 21. During the period, wind profiler and surface observations were available every hour, and rawindsondes were available every 12 hours. This assimilation cycle improved the positioning of the upper-level trough as it moved off the Rockies, and subsequently the positioning of the trough as well as squall line later on. Even without the assimilation cycle, the precipitation pattern associated with the tornadic supercells in the AR region at around 00 UTC January 22 was, however, very

similar. No data assimilation is performed on the 6-km grid. Its solution is a true forecast throughout the 48-hour period if one neglects the observational information fed in through the lateral boundary during the first 24 hours.

7.3. The results

Limited by space, we will only show plots near the time of tornado outbreak and at the end of 48 hours and compare the model-predicted flow and

precipitation patterns with the observed patterns. More detailed analysis and verification are deferred to a future paper.

The fields of model simulated/predicted 32-km mean sea-level pressure, surface wind and total (both grid-scale and parameterized cumulus) precipitation rate at 00 UTC January 22 and 12 UTC January 23 are shown in Fig. 9. They correspond to 12 and 48 hours from the model start time. The corresponding NCEP Eta analysis fields (except for precipitation rate) are shown in Fig. 10. As can

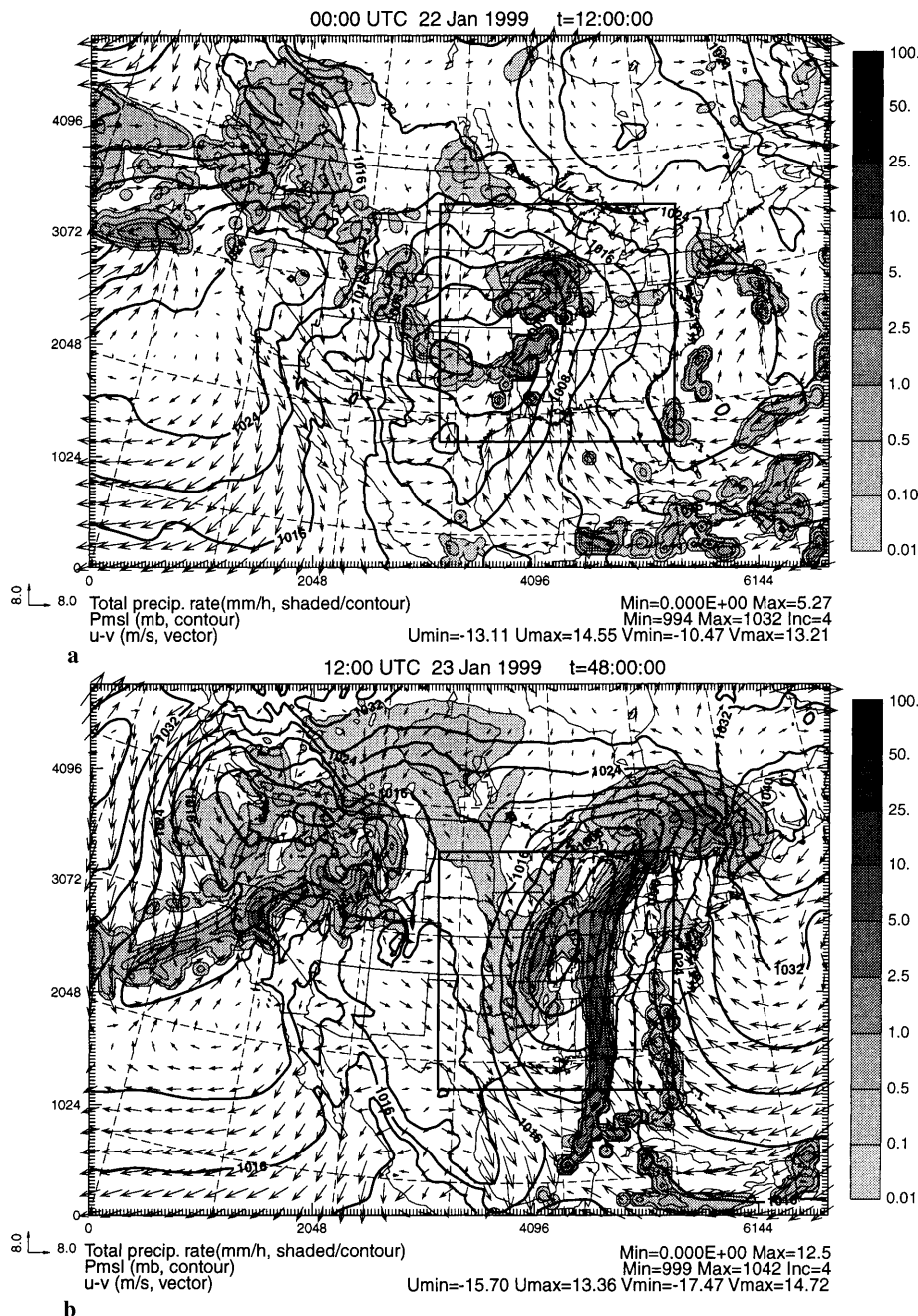


Fig. 9. ARPS simulation/forecast surface winds, mean sea-level pressure (contours) and total precipitation rate (shaded contours) at 00 UTC 22 January **a**, and 12 UTC 23 January 1999 **b** on the 32-km grid, corresponding to 12 h and 48 h from the model start time, respectively. The box indicates the location of 6-km nested grid

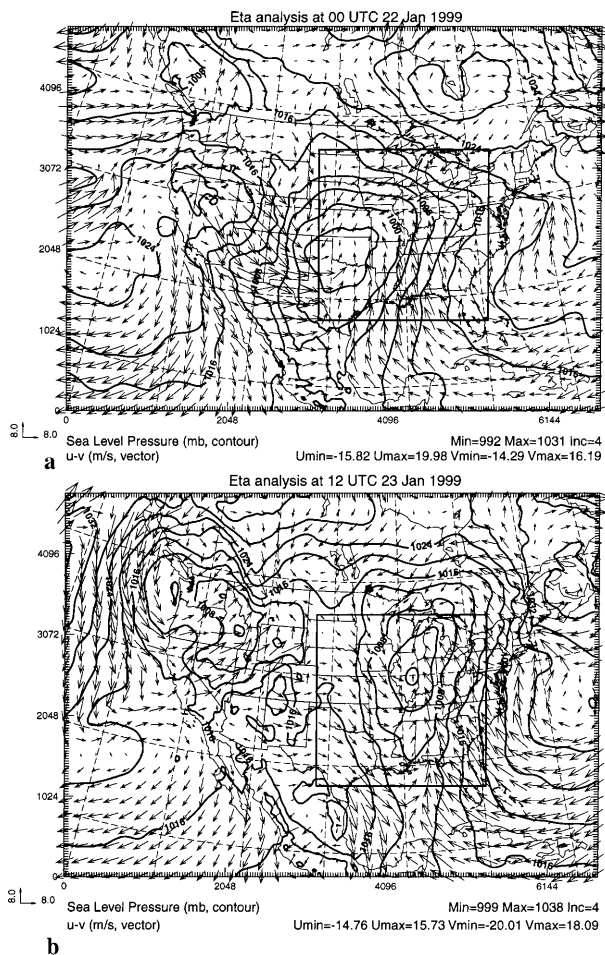


Fig. 10. NCEP Eta analysis surface winds, mean sea-level pressure (contours) and total precipitation rate (shaded contours) at **a** 00 UTC 22 January, and **b** 12 UTC 23 January 1999. The squared box indicates the location of 6-km ARPS grid

be seen, at 00 UTC January 22, the surface low is centered over SW OK and NW TX in both the ARPS simulation and the Eta analysis. The surface low is associated with a cyclonic circulation. A strong surface temperature gradient (not shown) is found extending from this circulation center northeastward along the strong convergence zone where a quasi-stationary front is analyzed (Fig. 8b). Extending southwestward from the circulation center into western TX is a cold front between west-northwesterly and southerly flows. Further south, another confluence zone is found between westerly and southerly flows and this convergence zone played a role in establishing the convection in the southern portion of the squall line later on. In general, the ARPS pressure and flow patterns match the Eta analysis very well.

The minimum pressure at the low center is slightly higher (by about 2 hPa) than the analysis, though.

At 00 UTC January 22, the low-level southerly flow is located in AR and supplies warm moist air from the Gulf to this area. The ARPS simulation (Fig. 9a) shows precipitation extending SW through NE across AR, agreeing very well with the satellite observations (Fig. 11a, b). Separately, it can be determined that a significant portion of the precipitation is of convective nature (not shown). In nature, the precipitation was generated from supercells that spawn a series of tornadoes. It is worth noting that the simulated precipitation in AR is not located along a surface convergence zone or a surface front. Detailed analysis shows that forcing associated with an upper-level baroclinic zone at the leading edge of mid- to upper-level temperature trough is responsible for the triggering of the convection. The convective line does coincide with the western boundary of a tongue of high CAPE associated with the southerly flow, though. The upper-cold front model of Browning and Monk (1982) or the cold front aloft model of Hoobs et al. (1996), and Locatelli et al. (1997) can be used to understand the dynamic process. In such a case, convective cells or rainbands form ahead of (and away from) a surface cold front or pressure trough but are closely related to the upper-level gradient in temperature and some times more prominently in equivalent potential temperature. Finally, the precipitation on the backside of the surface cyclone, that extending along the warm front eastward through NE US, and that extending along a quasi-stationary front from TX panhandle through Colorado to Wyoming are all well reproduced. The precipitation over the northwestern states and British Columbia also compares well with the satellite observations (Fig. 11a, b).

The ARPS predicted fields at 48 hours (12 UTC January 23) are shown in panel (b) of Fig. 9 while those of Eta analyses are shown in Fig. 10. As discussed earlier, the surface cyclone has evolved into an elongated shape and is centered in Illinois; this is true in both prediction and observation. The values of minimum pressure are nearly identical. The pressure gradient in the model is tighter on the western flank of the low, due to slightly stronger ridge found between two surface lows (the other one is centered over the Pacific

Northwest). The dominant weather at this time is an intense squall line extending from the Great Lakes area southward into the Gulf of Mexico. Strong convergence is found in the surface winds along the line, but the strongest temperature gradient remains behind the squall line and is associated with a surface cold front. Detailed analyses have revealed complicated interaction processes of the convective scale flows with those at the large scales, in particular with the upper-level jets; the vertical transport of horizontal momentum by the squall line circulation and the associated geostrophic adjustment significantly accelerated the upper-level jet which in turn modified the large-scale environment for the squall line. We also note that the forecast position of the squall line agrees very well with the observations, as is its earlier evolution.

On the northern portion of the squall line, a significant part of the precipitation is of stratiform nature. The low-level accelerating pre-squall line inflow is believed to strengthen the southerly flow through geostrophic adjustment, thereby enhancing the warm and moist air supply (in the form of warm conveyor belt) as well as the upward flow at the warm front to the north. Precipitation is also found on the backside of the surface cyclone where a cold front can be analyzed. Other regions of precipitation are found to be associated with the cyclone on the Pacific Northwest. The predicted precipitation regions to the east of the squall line, mostly along the southeast coast and over the ocean (also found at earlier times), are spurious however; they can be entirely attributed to the cumulus parameterization scheme. Apart from that, the predicted precipitation pattern agrees

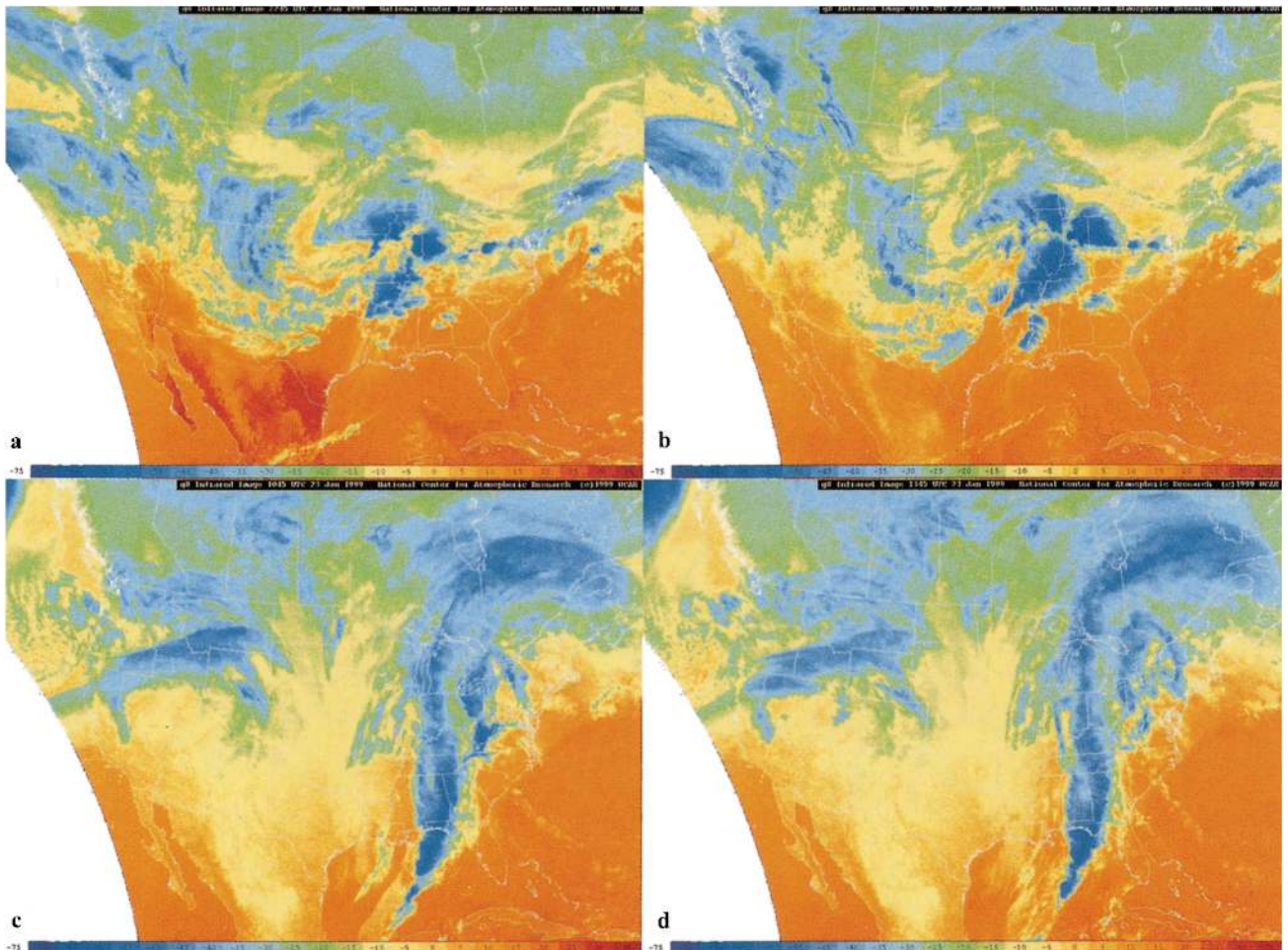


Fig. 11. Infrared satellite images of cloud top temperature at **a** 22:45 UTC January 21, **b** 1:45 UTC January 22, **c** 10:45 UTC, **d** 13:45 UTC January 23. Cold temperature indicates high cloud top and deep convection

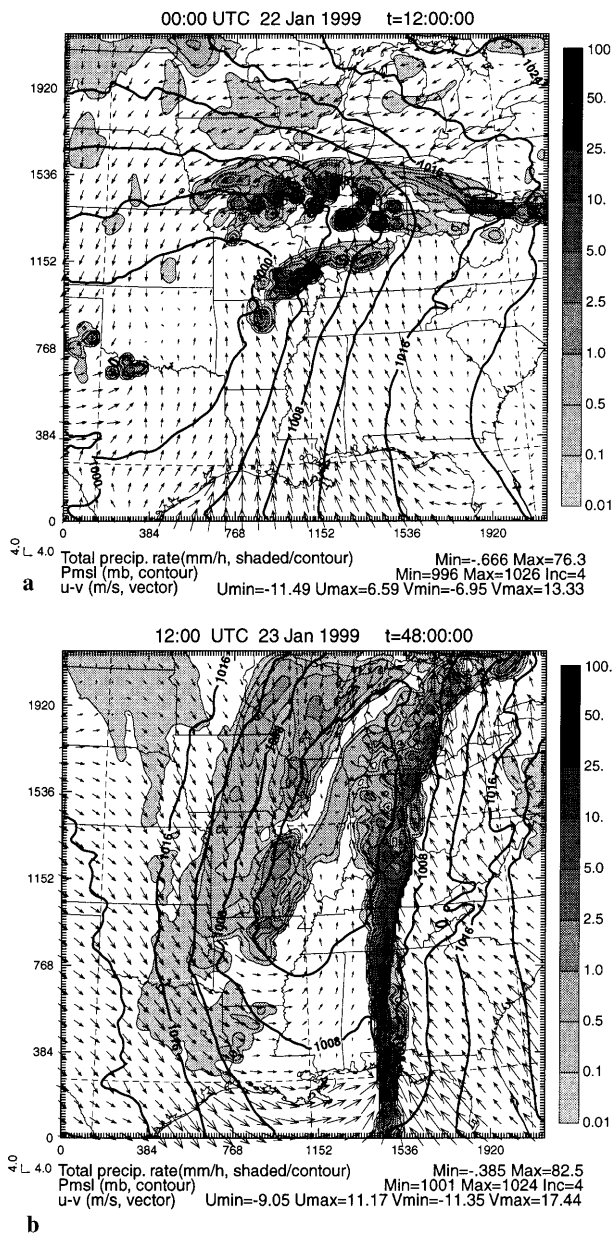


Fig. 12. ARPS 6-km forecast of surface winds, mean sea-level pressure (contours) and total precipitation rate (shaded contours) at **a** 00 UTC 22 January and **b** 12 UTC 23 January 1999, corresponding to 12 h and 48 h from the model start time, respectively

very well with the satellite observations (Fig. 11c, d).

The 6-km ARPS forecast of surface pressure, mean sea-level pressure and total precipitation rate at 00 UTC January 22, and 12 UTC January 23 are shown in Fig. 12. The 6-km results are true forecast starting from ADAS analysis at 12 UTC January 21. No data assimilation is performed on this grid. Boundary conditions are linearly inter-

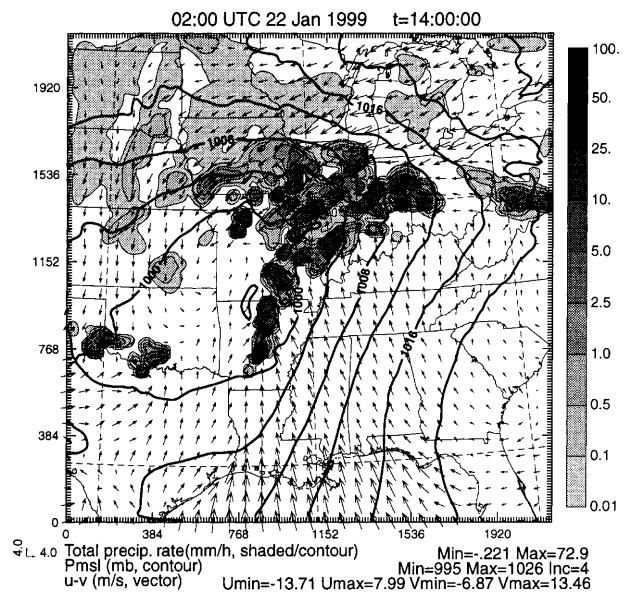


Fig. 13. As Fig. 12, but for 02 UTC 22 January 1999, corresponding to 14-hour forecast

polated from 32-km solutions at hourly intervals. The general patterns of flow, pressure and precipitation are similar to those of 32-km grid. The increased resolution resolves a lot more of the fine-scale details. Individual convective cells embedded within broader precipitation areas can be readily identified and the squall line is much narrower. At 12 UTC, the 6-km grid also correctly picked up two weaker bands, one narrower and one broader on the backside of the cyclone. These two bands match radar observations well (not shown). This grid did not produce the spurious precipitation over the ocean found in the 32-km grid. This grid missed, however, the pre-squall line precipitation near Lake Erie, which is seen in the satellite images and also in the 32-km forecast. Furthermore, the convection in SW AR is absent at 00 UTC January 22, suggesting that without the aid of cumulus parameterization, the explicit vertical lifting even on the 6-km grid is still too weak to trigger convection in a timely fashion. The convection is delayed by about three hours in that part of the domain. The convection does occur at a later time, as seen from the forecast of two hours later given in Fig. 13. This finding is further supported by the results of the nested 2-km grid in which convection does occur at the correct time, i.e., about three hours earlier than in the 6 km grid. A series of storms with strong, readily identifiable, low-level rotation were obtained on

the 2-km grid (not shown). Finally, we note that the surface cyclone on the 6-km grid is actually weaker than that on the 32-km grid. This error may have been caused by the reduced accumulated heating due to the delayed onset of convection. The longer forecasting range (48 hours versus 24 hours) with the 6-km grid may have also contributed to the larger error.

7.4. Summary

The 21–23 January 1999 case of Arkansas tornado outbreak and the central and eastern US squall line is simulated using the ARPS at 32-km and 6-km resolutions. These two grids cover a wide range of scales and make full use of the capabilities of the ARPS system. The latter include most physics options, the data analysis and assimilation capabilities and the capability of running on distributed-memory massively parallel computers. The results presented show that the model is capable of accurately reproducing flow and precipitation patterns from synoptic down to convective scales. The suggested predictability of intense squall lines up to 48 hours, at least for this particular case, is very encouraging. A 2-km grid nested in the 6-km grid is able to reproduce the supercell storm morphology and strong low-level rotation associated with the tornadoes, it also predicts the onset of initiation of these supercells with a better temporary accuracy. The results also suggest that certain cumulus parameterization is still needed at 6-km resolution in order to accurately predict the timing of convective initiation.

Many important processes are involved in this case and physical understanding of all these processes requires additional analyses, including quantitative diagnostics and trajectory analysis. Some of these have been completed and will be reported in a forthcoming paper. Quantitative precipitation verification will also be examined. The main purpose here is to demonstrate the ARPS capabilities in an NWP setting.

8. Other validation experiments

Without longitude and latitude dependent forcing, the solution of the ARPS should remain axis or slab symmetric if the grid configuration and the initial condition are symmetric. Symmetry tests

have proven to be perhaps one of the most effective ways of discovering coding errors, as was also found by Clark (1979).

In ARPS, symmetry tests are performed by specifying initially symmetric random perturbations in the potential temperature field. They are designed to check as many subroutines and options as possible. Separate tests are performed for 3-D, 2-D, x-z and y-z plane configurations. When conducted on 64-bit machines, the symmetry is typically maintained up to the 10th digit after the decimal point in the velocity fields after several hundred of time steps. On 32-bit machines, the symmetry is usually maintained up to the 6th digit after the decimal place.

The stability and accuracy of the time integration of ARPS was also tested with a procedure described in Skamarock and Klemp (1994). In these tests, small amplitude (linear) inertia-gravity waves were simulated in a 2-D periodic channel, with rigid free-slip upper and lower boundaries. Inertia-gravity waves were excited by a small initial perturbation in potential temperature, inside a Bousinesq flow of constant static stability and flow speed. The time-dependent analytical solutions can be obtained. Model solutions for both nonhydrostatic (short) and inertia gravity waves were obtained with the ARPS, and were similar in accuracy to that of Skamarock and Klemp (1994).

The integrity of the dynamical portion of the ARPS is further tested by applying it to a three-dimensional nonlinear viscous Beltrami flow, for which exact solution to the Navier-Stokes can be found. Shapiro (1993) showed that at the end of two e-folding time of decay, the maximum relative error in the solutions obtained on a $90 \times 60 \times 45$ grid is about 3%. Finally, the ARPS, after being modified to match the treatment of advection and SGS turbulence in the Klemp and Wilhelmson (1978) model as documented in Wilhelmson and Chen (1982), produces closely matched solutions to the Klemp and Wilhelmson model, even for highly non-steady multi-cellular storms up to several cell regeneration periods.

9. General summary

In this paper, the treatment of the land surface processes, the coupling of PBL with the land sur-

face model and the treatment of explicit and parameterized precipitation processes in the ARPS system are presented. The model is validated in this paper and Part I using a wide range of problems in various different configurations. These results also serve to demonstrate the capabilities of the ARPS as a general-purpose multi-scale atmospheric research and prediction tool. As is stated in the summaries for individual test cases, the model is able to reproduce known, and in some cases analytical, solutions with high accuracy. The paper culminates at the simulation of a real data case that makes use of most of the capabilities of the system. Certain insights have also been gained in the physical understanding of this case.

In the end, we note that all features and capabilities of the ARPS system are not exercised in the experiments and tests presented in the current two-part paper. Other features of ARPS include the Doppler velocity retrieval and thermodynamic retrieval packages, cloud analysis capabilities of the ADAS, data assimilation using incremental analysis update, and movable grid two-way interactive nesting through the adaptive grid refinement strategy.

Acknowledgement

The Center for Analysis and Prediction of Storms was supported by the National Science Foundation and Federal Aviation Administration through combined Grant and Cooperative Agreement ATM92-20009. A special acknowledgement is in order for our colleagues who contributed in various ways to the development and testing of the ARPS. They include Hao Jin, Xiaoguan Song, Adwait Sathye, Gene Bassett, Richard Carpenter, David Jahn, Min Zou, Limin Zhao, Jinxing Zong, Steve Weygandt, Jason Levit, Steve Lazarus, Jian Zhang, Yvette Richardson, Leilei Wang, Scot Ellis, Yifang Tang, John Mewes, William Martin, Yunyun Lu and Seon-Ki Park.

We have benefited greatly from collaborations and discussions with numerous scientists, including: Drs. William Skamarock, Andrew Crook, Jimmy Dudhia, Gregory Tripoli, Wei-Kuo Tao, Louis Wicker, Greg Mattocks on various issues. Our special acknowledgement go to Dr. Wei-Kuo Tao for providing the original ice microphysics and NASA radiation code used in the Goddard cumulus ensemble model, to Dr. William Skamarock for collaborative work on the adaptive grid refinement interface, to Paul Schultz for letting us use his ice scheme. Graphics are produced by ZXPLLOT developed by the lead author and Zuojun Zhang. We also acknowledge the Oklahoma Climate Survey for making available the Mesonet data.

References

- Anderson RJ (1993) A study of wind stress and heat flux over the open ocean by the inertial dissipation method. *J Phys Oceanogr* 23: 2153–2161
- Andre JC, DeMoor G, Lacarcere P, Therry G, Vachat Rd (1978) Modeling the 24-hour evolution of the mean and turbulent structures of the planetary boundary layer. *J Atmos Sci* 35: 1862–1883
- Andre JC, Goutorbe JP, Perier A (1986) HAPEX-MOBILHY: A hydrological atmospheric experiment for the study of water budget and evaporation flux at the climate scale. *Bull Amer Meteor Soc* 67: 138–144
- Bergeron T (1935) On the physics of cloud and precipitation. *Proc 5th Assembly of IUGG, Lisbon*, 156–178
- Boone A, Calvet J-C, Noilhan J (1999) Inclusion of a third soil layer in land surface scheme using the force-restore method. *J Appl Meteor* 38: 1611–1630
- Brewster K (1996) Application of a Bratseth analysis scheme including Doppler radar data. Preprints, 15th Conference on Weather Analysis and Forecasting. Amer Meteor Soc, Norfolk, VA, 92–95
- Brock FV, Crawford KC, Elliott RL, Cuperus GW, Stadler SJ, Johnson HL, Eilts MD (1995) The Oklahoma Mesonet: A technical overview. *J Atmos Oceanic Tech* 12: 5–19
- Browning KA, Monk GA (1982) A simple model for the synoptic analysis of cold fronts. *Quart J Roy Meteor Soc* 108: 435–452
- Byun DW (1990) On the analytical solution of flux-profile relationships in the atmospheric surface layer. *J Appl Meteor* 29: 652–657
- Chou M-D (1990) Parameterization for the absorption of solar radiation by O₂ and CO₂ with application to climate studies. *J Climate* 3: 209–217
- Chou M-D (1992) A solar radiation model for climate studies. *J Atmos Sci* 49: 762–772
- Chou M-D, Suarez MJ (1994) An efficient thermal infrared radiation parameterization for use in general circulation models, NASA Tech Memo 104606, 85 pp. [Available from NASA Center for Aerospace Information, 800 Elkridge Landing Road, Linthicum Heights, MD 21090-2934]
- Clark TL (1979) Numerical simulations with a three-dimensional cloud model: Lateral boundary condition experiments and multicellular severe storm simulations. *J Atmos Sci* 36: 2192–2215
- Clarke RH, Dyer AJ, Brook RR, Reid DG, Troup AJ (1971) The Wangara experiment: Boundary layer data. *Div Meteor Phys, CSIRO [NTIS N71-37838]*
- Deardorff JW (1972) Parameterization of the planetary boundary layer for use in general circulation models. *Mon Wea Rev* 100: 93–106
- Deardorff JW (1980) Stratocumulus-capped mixed layers derived from a three-dimensional model. *Bound Layer Meteor* 18: 495–527
- Hobbs PV, Locatelli JD, Martin JE (1996) A New Conceptual Model for Cyclones Generated in the Lee of the Rocky Mountains. *Bull Amer Meteor Soc* 77: 1169–1178

- Jacquemin B, Noilhan J (1990) Sensitivity study and validation of a land surface parameterization using the HAPEX-MOBILHY data set. *Bound Layer Meteor* 52: 93–134
- Kain JS, Fritsch JM (1990) A one-dimensional entraining/detraining/detraining plume model and its application in convective parameterization. *J Atmos Sci* 47: 2784–2802
- Kain JS, Fritsch JM (1993) Convective parameterization for mesoscale models: The Kain-Fritsch scheme, The Representation of Cumulus Convection in Numerical Models. *Meteor Monogr Amer Meteor Soc*, 165–170
- Kessler E (1969) On the Distribution and Continuity of Water Substance in Atmospheric Circulations, 84 pp
- Kidwell KBE (1990) Global Vegetation Index User's guide, USDOC/NOAA National Climate Data Center, Satellite Data Services Division, Washington DC
- Kineman JJ, Ohrenschall MA (1992) Global Ecosystem Database (CD-ROM) Version 1.0 Documentation Manual. EPA/600/R-96/194b, NGDC Key to Geophysical Records Documentation No 27, National Geophysical Data Center, NOAA, Boulder, CO
- Klemp JB, Rotunno R (1983) A study of the tornadic region within a supercell thunderstorm. *J Atmos Sci* 40: 359–377
- Klemp JB, Wilhelmson RB (1978) The simulation of three-dimensional convective storm dynamics. *J Atmos Sci* 35: 1070–1096
- Klemp JB, Wilhelmson RB, Ray PS (1981) Observed and numerically simulated structure of a mature supercell thunderstorm. *J Atmos Sci* 38: 1558–1580
- Kuo HL (1965) On the formation and intensification of tropic cyclones through latent heat release by cumulus convection. *J Atmos Sci* 22: 40–63
- Kuo HL (1974) Further studies of the parameterization of the influence of cumulus convection on large-scale flow. *J Atmos Sci* 31: 1232–1240
- Lafore JP, Stein J, Asencio N, Bougeault P, Ducrocq V, Duron J, Fisher C, Péreil P, Mascart P, Masson V, Pinty JP, Redelsperger JL, Richard E, Vilà-Guerau de Arellano J (1998) The meso-NH atmospheric simulation system. Part I: Adiabatic formulation and control simulation. *Ann Geophysicae* 16: 90–109
- Lin Y, Ray PS, Johnson KW (1993) Initialization of a modeled convective storm using Doppler radar-derived fields. *Mon Wea Rev* 121: 2757–2775
- Lin Y-L, Farley RD, Orville HD (1983) Bulk parameterization of the snow field in a cloud model. *J Climate Appl Meteor* 22: 1065–1092
- Locatelli JD, Stoelinga MT, Schwartz RD, Hobbs PV (1997) Surface convergence induced by cold fronts aloft and prefrontal surges. *Mon Wea Rev* 125: 2896–2916
- Mahfouf J-F, Noilhan J, Peris P (1984) Simulations du bilan hydrique avec ISBA, application au cycle annuel dans le cadre de PILPS. Atelier de Mondélisation de l'atmosphère, Toulouse, France
- Marshall JS, Palmer WM (1948) The distribution of raindrops with size. *J Meteor* 5: 165–166
- Moeng C-H (1984) A large-eddy-simulation model for the study of planetary boundary layer turbulence. *J Atmos Sci* 41: 2052–2062
- Monin AS, Obukhov AM (1954) Basic laws of mixing in the ground layer of the atmosphere. *Tr Geofiz Inst Akad Nauk SSSR* 151: 163–187
- Noilhan J, Planton S (1989) A simple parameterization of land surface processes for meteorological models. *Mon Wea Rev* 117: 536–549
- NSSC (1994) State Soil Geographic (STATSGO) Data Base. Miscellaneous Publication Number 1492, National Soil Survey Center, United States Department of Agriculture
- Oke TR (1978) *Boundary Layer Climates*. London: Methuen and Sons, 372 pp
- Orlanski I (1976) A simple boundary condition for unbounded hyperbolic flows. *J Comput Phys* 21: 251–269
- Pleim JE, Xiu A (1995) Development and testing of a surface flux and planetary boundary layer model for application in mesoscale models. *J Appl Meteor* 34: 16–32
- Ray PS, Johnson B, Johnson KW, Bradberry JS, Stephens JJ, Wagner KK, Wilhelmson RB, Klemp JB (1981) The morphology of severe tornadic storms on 20 May 1977. *J Atmos Sci* 38: 1643–1663
- Raymond DJ, Emanuel KA (1993) The Kuo cumulus parameterization, The representation of cumulus convection in numerical models. *Meteor Monogr Amer Meteor Soc*, 145–147
- Rutledge SA, Hobbs PV (1984) The mesoscale and microscale structure and organization of clouds and precipitation in midlatitude cyclones. Part XII: A diagnostic modeling study of precipitation development in narrow cold-frontal rainbands. *J Atmos Sci* 41: 2949–2972
- Schultz P (1995) An explicit cloud physics parameterization for operational numerical weather prediction. *Mon Wea Rev* 123: 3331–3343
- Sellers PJ, Hall FG, Asrar G, Strebel DE, Murphy RE (1992) An overview of the first International Satellite Land Surface Climatology Project (ISLSCP) Field Experiment (FIFE). *J Geophys Res* 97: 18345–18371
- Shapiro A (1993) The use of an exact solution of the Navier-Stokes equations in a validation test of a three-dimensional nonhydrostatic model. *Mon Wea Rev* 121: 2420–2425
- Skamarock W, Klemp JB (1994) Efficiency and accuracy of the Klemp-Wilhelmson time-splitting technique. *Mon Wea Rev* 122: 2623–2630
- Soong S-T, Ogura Y (1973) A comparison between axisymmetric and slab-symmetric cumulus cloud models. *J Atmos Sci* 30: 879–893
- Sun W-Y, Chang C-Z (1986) Diffusion model for a convective layer. Part I: Numerical simulation of convective boundary layer. *J Climate Appl Meteor* 25: 1445–1453
- Tao W-K, Lang S, Simpson J, Sui C-H, Ferrier B, Chou M-D (1996) Mechanism of cloud-radiation interaction in the tropics and mid-latitude. *J Atmos Sci* 53: 2624–2651
- Tao W-K, Simpson J (1993) Goddard cumulus ensemble model. Part I: Model description. *Terres Atmos Ocean Sci* 4: 35–72
- Tao W-K, Simpson J, McCumber M (1989) An ice-water saturation adjustment. *Mon Wea Rev* 117: 231–235
- Wilhelmson RB, Chen C-B (1982) A simulation of the development of successive cells along a cold outflow boundary. *J Atmos Sci* 39: 1466–1483

- Xue M, Droegemeier KK, Wong V (2000) The Advanced Regional Prediction System (ARPS) – A multiscale non-hydrostatic atmospheric simulation and prediction tool. Part I: Model dynamics and verification. *Meteor Atmos Physics* 75: 161–193
- Xue M, Droegemeier KK, Wong V, Shapiro A, Brewster K (1995) ARPS Version 4.0 User's Guide. Center for Analysis and Prediction of Storms, [Available from CAPS, Univ of Oklahoma, 100 E Boyd St, Norman OK 73019], 380 pp
- Xue M, Droegemeier KK, Woodward PR (1993) Simulation of tornado vortices within a supercell storm using adaptive grid refinement technique. Preprints, 17th Conf on Severe Local Storms, St Louis, MO. Amer Meteor Soc, 362–365
- Xue M, Zong J, Droegemeier KK (1996) Parameterization of PBL turbulence in a multi-scale nonhydrostatic model. Preprint, 11th AMS conference on Numerical Weather Prediction. Amer Meteor Soc, Norfolk, VA, 363–365
- Zalesak ST (1979) Fully multi-dimensional flux-corrected transport algorithms for fluids. *J Comput Phys* 31: 335–362
- Author's address: Dr. Ming Xue, School of Meteorology, University of Oklahoma, Sarkeys Energy Center, Suite 1110, 100 East Boyd, Norman, OK 73019 (E-mail: mxue@ou.edu)